ENVIRONMENTAL SCIENCES Vol. 1, No. 2, 105~117
Bulletin of the Korean Environmental Sciences Society

A Numerical Study on the Karman Vortex Generated by Breaking of Mountain Wave

Sung-Dae Kang and Fujio Kimura

Institute of Geoscience, University of Tsukuba, Ibaraki, Japan

(Manuscript received on 22 October, 1997)

The formation mechanism of the vortex streets in the lee of the mountain is investigated by a three-dimensional numerical model. The model is based upon the hydrostatic Boussinesq equations in which the vertical turbulent momentum flux is estimated by a turbulence parameterization scheme, but the horizontal viscosity is assumed to be constant.

The results show that Karman vortex streets can form even without surface friction in a constant ambient flow with uniform stratification. The vortex formation is related to breaking of the mountain wave, which depends on the Froude number (Fr). In the case of a three-dimensional bell-shaped mountain, the wave breaking occurs when Fr is less than about 0.8, while a Karman vortex forms when Fr is less than about 0.22. Vortex formation also depends on Reynolds number, which is estimated from the horizontal diffusivity.

The vortex formation can be explained by the wave saturation theory given by Lindzen (1981) with some modification. Simulations in this study show that in the case of Karman vortex formation the momentum flux in the lower level is much larger than the saturated momentum flux, whereas it is almost equal to the saturated momentum at the upper levels as expected from the saturation theory. As a result, large flux divergence is produced in the lower layer, the mean flow is decelerated behind the mountain, and the horizontal wind shear forms between unmodified ambient wind. The momentum exchange between the mean flow and the mountain wave is produced by the turbulence within a breaking wave. From the result, well developed vortices like Karman vortex can be formed.

The results of the momentum budget calculated by the hydrostatic model are almost the same as nonhydrostatic results as long as horizontal scale of the mountain is 10 km. A well developed Karman vortex similar to the hydrostatic one was simulated in the nonhydrostatic case. Therefore, we conclude that the hydrostatic assumption is adequate to investigate the origin of the Karman vortex from the viewpoint of wave breaking.

1. Introduction

Mesoscale eddy streets in the lee of islands are often observed in satellite photographs. Figure 1 shows well developed Karman vortex streets in the lee of Che-Ju island. Hubert and Krueger (1962) found that there are some eddy patterns in photographs. They discussed the formation mechanism and pointed out that gravity waves accompanied with a low inversion layer should be important. Many researcher (Chopra and Hubert, 1965, Tsuchiya, 1969) discussed the similarity to the Karman vortex streets behind cylinders in laboratories. They found that characteristic parameters of the eddies, such as the lateral and longitudinal spacing and rate of shedding of eddy pairs, agree well with those of laboratory Karman vortex streets. They concluded that the formation mechanism of the eddies in the atmosphere is the same as the laboratory Karman vortices except for the molecular viscosity, which must be replaced by the lateral eddy viscosity. They also suggested that it is possible to estimate the eddy viscosity

Fig. 1. Satellite image for 18Z 4 February 1987. Che-Ju island can be seen in the central part of the photograph. Karman vortex is observed in the lee of Che-Ju island.

from the characteristic parameters of the atmospheric eddies. Atkinson (1981) summarized the eddy viscosity estimated by the method mentioned above.

Rusher and Deardorff (1982) carried out a numerical simulation of vortex streets by using a two-dimensional mixed-layer model, which included topography and surface friction. Characteristics of the simulated eddies were similar to those in the atmosphere, but the tendency on the horizontal diffusivity was not clear. Yagi et al. (1987) studied vortex streets by use of a linear solution and showed that vortex streets are formed in the horizontal-shear flow by shear instability. He also showed that lee vortex streets can form without surface friction in the lee of a mountain by using a two-dimensional shallow-flow numerical model.

By laboratory experiments, Brighton (1978) showed that the features of the lee vortices depend on the strength of the stratification. Smolarkiewicz and Rotunno (1989) studied stratified flow over an isolated mountain with a three-dimensional non-hydrostatic model. They found that a stationary vortex pair can form without surface friction and that the mechanism is associated with the dynamics of gravity waves. This fact implied that atmospheric vortex streets in lee of islands may be also formed without surface friction. They explained that the vortex pair is generated by a baroclinic process which is non-linear but isentropic. Potential vorticity is conserved by this theory, so that it seems to be difficult to use this mechanism to explain the formation of vortex streets, which can exist far from the mountain.

Mesoscale eddies are also observed inland (Harada, 1981). These eddies, however, are not formed only by pure mechanical process. Kimura (1986) and McGregor and Kimura (1989) studied the eddies observed in Japan and in Australia, respectively, using a numerical model and found that the thermal effect of the mountain located windward of the vortex is important. The mechanical effect of the mountain, which is similar to the formation mechanism of the eddies in the lee of the isolated island, is important for some eddies. Satomura (1986) investigated instability of shear flow in shallow water and suggested that some topography can form mesoscale vortex in horizontal shear flow.

Spelt and Etling (1989a) and (1989b) reviewed the vortex streets observed in the atmosphere and laboratory and also those simulated by numerical models. They pointed out that it must be investigated whether the formation mechanism presented by Smolarkiewicz and Rotunno (1989) is also effective in atmospheric flow with a convective boundary layer under elevated inversion. They also pointed out that the formation of the vortex depends not only on Fr but also on Rossby number, so that further investigation of the effects of Coriolis parameter must be done.

In the reply to the Smith's (1989) comment, Smolarkiewicz and Rotunno (1989) showed a time-dependent calculation illustrating that lee vortices (reversed flow, circulating motion, etc) can form before PV (Potential Vorticity) is produced, and that therefore PV production is a result, rather than a cause of lee-vortex formation. This mean there is another mechanism which can become the origin of lee-vortex formation.

Several, more recent numerical studies have examined additional aspects of the flow of a stratified fluid past a tall isolated obstacle. These studies have demonstrated that the transition from the "flow over" to the "flow around" regime shows some of the characters of a bifurcation (Smith, 1993), in which the dimensionless mountain height (inverse of Froude number) acts as a control parameter. Other aspects of the flow-around problem have been studied using the concept of gravity-wave breaking (Durran, 1995; Olafsson and Bougeault, 1996, 1997; Schar and Durran, 1997).

In this study, the formation mechanism of the vortex streets is investigated by a three-dimensional hydrostatic model. The vortex formation can be expected to be related to the breaking of a mountain wave, so that the model must have sufficient accuracy to simulate mountain waves.

2. Numerical model

The governing equations and numerical scheme of the model are the same those developed by Kikuchi et al. (1981), and modified by Kimura and Arakawa (1983). The governing equations are Boussinesq hydrostatic equations which are written in a terrain-following coordinate system as follows:

Equation of motion:

$$\frac{\partial hu}{\partial t}+\frac{\partial huu}{\partial x}+\frac{\partial huv}{\partial y}+\frac{\partial huw^*}{\partial z^*} =$$
$$-h\Theta\frac{\partial \Pi'}{\partial x}+gh\frac{\theta'}{\Theta}\frac{z_T-z^*}{z_T}\frac{\partial z_G}{\partial x}+\frac{\partial}{\partial x}(hK_H\frac{\partial u}{\partial x})$$
$$+\frac{\partial}{\partial y}(hK_H\frac{\partial u}{\partial y})+\frac{z_T^2}{h}\frac{\partial}{\partial z^*}(hK_v\frac{\partial u}{\partial z^*}) , \quad (2.1)$$

$$\frac{\partial hv}{\partial t}+\frac{\partial hvu}{\partial x}+\frac{\partial hvv}{\partial y}+\frac{\partial hvw^*}{\partial z^*} =$$
$$-h\Theta\frac{\partial \Pi'}{\partial y}+gh\frac{\theta'}{\Theta}\frac{z_T-z^*}{z_T}\frac{\partial z_G}{\partial y}+\frac{\partial}{\partial x}(hK_H\frac{\partial v}{\partial x})$$
$$+\frac{\partial}{\partial y}(hK_H\frac{\partial v}{\partial y})+\frac{z_T^2}{h}\frac{\partial}{\partial z^*}(hK_v\frac{\partial v}{\partial z^*}) , \quad (2.2)$$

Equation of thermodynamics:

$$\frac{\partial h\theta'}{\partial t}+\frac{\partial h\theta' u}{\partial x}+\frac{\partial h\theta' v}{\partial y}+\frac{\partial h\theta' w^*}{\partial z^*} =$$
$$\frac{\partial}{\partial x}(hK_H\frac{\partial \theta'}{\partial x})+\frac{\partial}{\partial y}(hK_H\frac{\partial \theta'}{\partial y})$$
$$+\frac{z_T^2}{h}\frac{\partial}{\partial z^*}(hK_v\frac{\partial \theta'}{\partial z^*}) , \quad (2.3)$$

Continuity equation:

$$\frac{\partial hu}{\partial x}+\frac{\partial hv}{\partial y}+\frac{\partial hw^*}{\partial z^*} = 0 , \quad (2.4)$$

Hydrostatic equation:

$$\frac{\partial \Pi'}{\partial z^*} = \frac{h}{z_T}\frac{g\theta'}{\Theta^2} , \quad (2.5)$$

where z^* is the terrain-following vertical coordinate and is defined as:

$$z^* = z_T(z-z_G)/h \text{ and } h = z_T-z_G , \quad (2.6)$$

in which z_T and z_G are the levels of the top and the ground surface of the model atmosphere, respectively.

3. Computational domain and boundary conditions

The computational domain is a rectangle shown in Fig. 2, which is covered by 110 grid points in the x direction and 66 in the y direction. The model atmosphere is divided into 42 levels with uniform interval of 170 m except for the lowest layer, whose thickness is 10 m. The boundary conditions for momentum and heat equations at the ground surface are assumed to be those of free slip and heat insulation.

The radiation condition given by Orlanski (1976) is adopted for windward and leeward lateral boundaries. To suppress the computational mode generated at the lateral boundary, horizontal diffusivity increases exponentially forward the boundary. The maximum diffusivity does not exceed ten times that in the central part of the domain, because a too large diffusivity sometimes destabilizes the radiation-condition scheme. Side boundaries (y-direction) are assumed to be periodic.

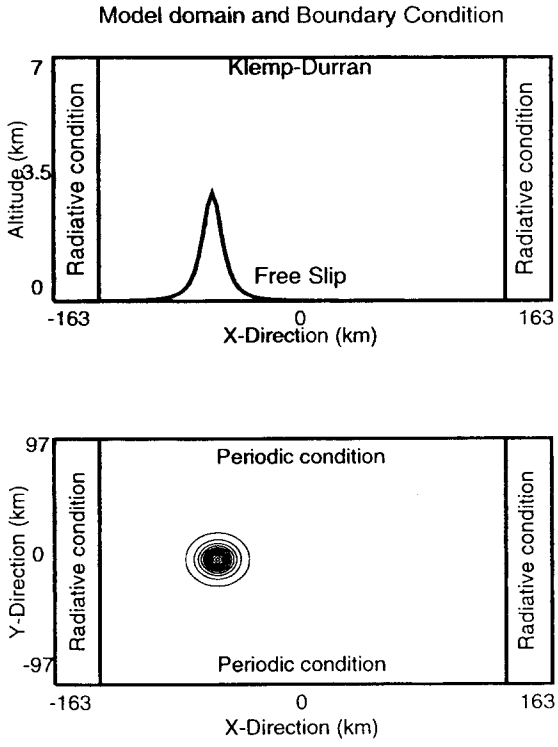

Fig. 2. Computational domain and boundary conditions, a side view (top) and a plane (bottom).

The top boundary should be treated carefully because internal gravity waves are very important for formation of the vortex streets as mentioned later. Gravity wave radiation condition given by Bougeault (1983) and Klemp and Durran (1983) is adopted for the top boundary, so that the internal waves propagating upward are absorbed at the top boundary without reflection.

The shape of a mountain is given by the following equation:

$$z_G = \frac{h}{(1+r^2/a^2)^{3/2}}, \tag{3.1}$$

where $r^2 = (x-x_0)^2 + (y-y_0)^2$, x_0 and y_0 are coordinates of the center of the mountain, and a is its half width. Since an analytical linear solution for internal waves over this mountain has been given by Smith (1980), the numerical solution can be verified for sufficiently low mountain height. Radius of the mountain a and grid interval (Δx) are assumed to be 10 km and 3 km, respectively.

4. Comparison with linear theory

Figure 3a shows horizontal contours of vertical velocity at the level of 1325 m normalized by Nh/a, where U is the ambient wind velocity (air flow is from left to right in the figure).

In this study, the Reynolds number (Re) is deformed as

$$Re = \frac{2aU}{K_H} = \frac{2aU}{0.02U\Delta x} \tag{4.1}$$

implying the Reynolds number of 333 in the numerical simulation. Brunt-Vaisala frequency N and ambient velocity U are assumed to be 0.01 s^{-1} and 10 ms^{-1}, respectively. The mountain height is chosen to be 100 m so that Fr is 7.4, the value at linear model should be accurate. Figure 3b shows the same contours obtained by the linear model. The horizontal distribution of the vertical velocity by the numerical model agrees quite well with that of the linear model.

Total downward momentum flux F_T (defined in sec. 7) of the mountain waves normalized by that given by the inviscid linear theory (F_L) is shown in Fig. 4a in cases of Re = 333, 250, and 200. As predicted by the linear theory, the total momentum flux is constant with height, and equal to (Smith, 1989):

$$F_L = \rho\frac{\pi}{4} NUh^2a \ . \qquad (4.2)$$

The figure shows that the fluxes given by the numerical model decrease slowly with height. The decrease rate is larger in case of smaller Re number, i.e., larger horizontal diffusivity. The reason for the decrease is the dissipation by the horizontal diffusion, and truncation error of finite-difference approximation also may contribute to some degree. In the case of Re = 333, the momentum flux is almost equal to the linear value at the surface, but decreases to about 81 percent at the level of 2.5 *km*.

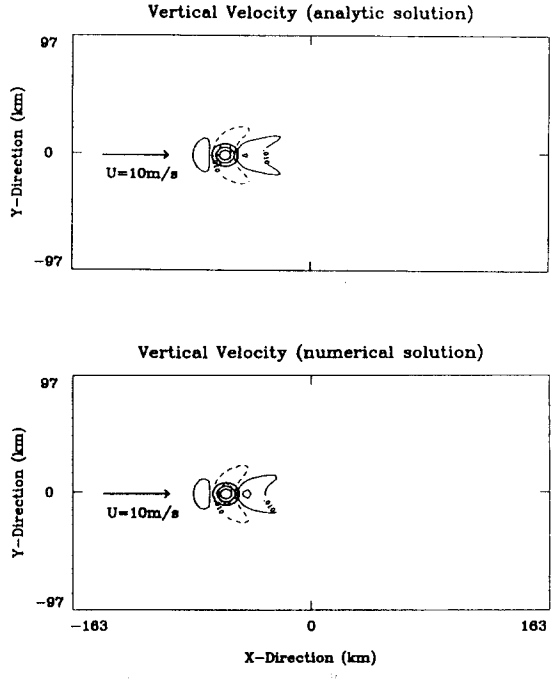

Fig. 3. (a) Horizontal contours of vertical component of the velocity at the level of 1325 m, normalized by Nh/a. Mountain height is 100 m (Fr=7.4). (obtained by the numerical model), (b) The same figure as (a), but given by the analytical linear model.

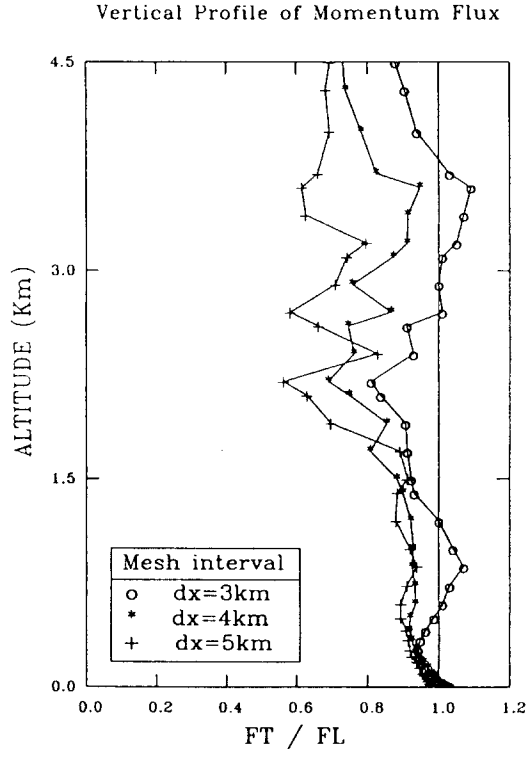

Fig. 4a.

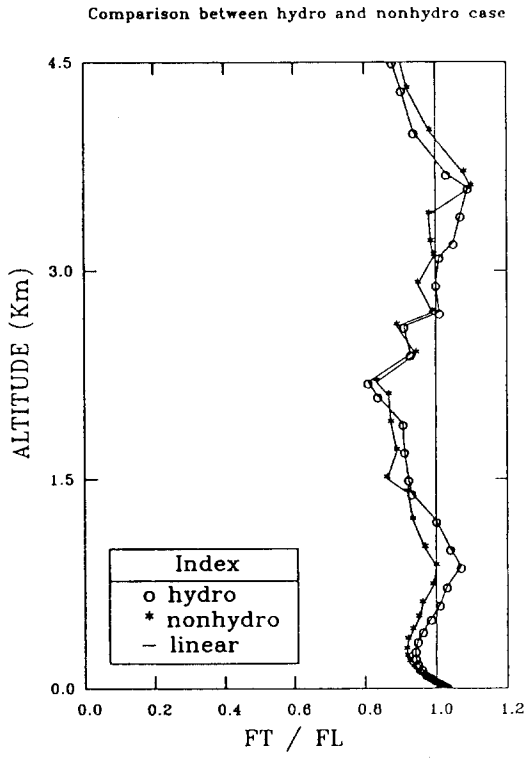

Fig. 4b.

Fig. 4. (a) Vertical profiles of momentum flux normalized by F_L, which is momentum flux given by the linear theory (eq.4.2). Three cases with different Re number (333, 250 and 200) are plotted. Mountain height is 100 m ($Fr=7.4$). (b) Comparison of momentum fluxes between hydrostatic and nonhydrostatic result in case of $\Delta x = 3$ km.

5. Accuracy of the hydrostatic assumption

Vertical momentum flux shown in Fig. 4a ($\Delta x = 3$ km case), which is obtained under the hydrostatic assumption, is compared with a nonhydrostatic result.

Figure 4b shows the vertical profile of total downward momentum fluxes F_T normalized by the inviscid linear momentum flux (F_L) in cases of both hydrostatic and nonhydrostatic assumption. The figure shows that the vertical profile of momentum fluxes calculated by the hydrostatic model is almost the same as in the nonhydrostatic case. Well developed Karman vortex similar to Fig. 5e was simulated with a nonhydrostatic model (no figure here). Therefore, hydrostatic model is sufficient to study the origin of Karman vortex from the viewpoint of wave breaking as long as the horizontal scale of a mountain is greater or equal to 10 km.

6. Vortex formation

Figures 5a-5e show streamlines at $z^* =$ 1000 m for the case of $Re = 333$, $U =$ 10 ms^{-1} and $N = 0.014$ s^{-1} for mountain height of 200 m, 500 m, 1000 m, 1500 m, and 3200 m, respectively. To emphasize the disturbance, 75 percent of the ambient velocity U has been subtracted from the velocity field. Figure 5a shows the three dimensional hydrostatic mountain waves, which have been analyzed by Smith (1980) with a linear model. No vortex forms in this case. The wave-like disturbance becomes larger with the increase of mountain height (see Fig. 5b and 5c), and a pair of lee vortices forms when mountain height is 1.5 km (see Fig. 5d). The vortex pair seems to be almost stationary. Figure 5e ($h = 3.2$ km) shows a vortex street which resembles the Karman vortex in the real atmosphere. This result shows that the vortex forms without either inversion or surface friction.

As mentioned above when Fr number is large enough, the solution is close to the linear mountain waves. If Fr number becomes smaller, then wave breaking occurs, namely, the vertical gradient of the isothermal surface becomes large,

and then Ri number becomes small generating turbulence which gives large vertical diffusivity over the mountain. For even smaller Fr number, a pair of stationary vortices forms in the lee of the mountain. The non-stationary vortex street forms only when Fr is less than about 0.22. In case of Re = 250, however, it is difficult to find moving vortices like the Karman vortex, though the flow is not completely stationary in the lee of the mountain. When Re is 200, only a pair of stationary vortices can be seen in the lee of the mountain. The periodic lateral boundary sometimes interrupts the vortex formation. To form the vortex, the distance between the boundaries must be at least 17−20 times larger than a, the radius of the mountain.

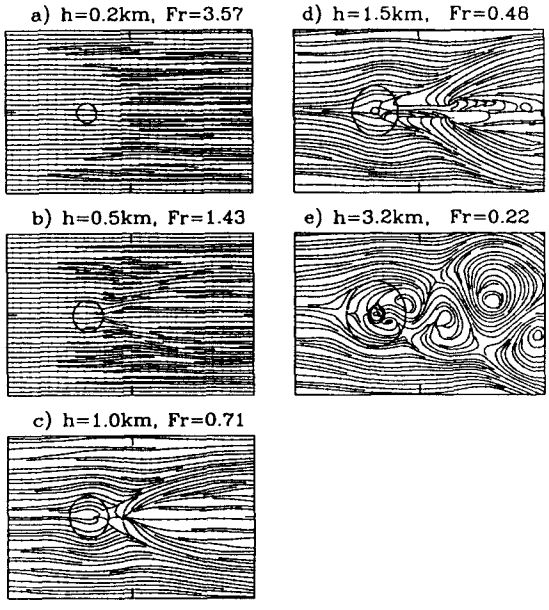

Fig. 5. Streamlines at the level of 1 *km*, for the case Re = 333, U = 10 ms^{-1}, N = 0.014 s^{-1} in which 75 percent of the ambient velocity U has been subtracted in order to emphasis the disturbance. Mountain height and Fr number are shown in each figures indicated by $a-e$.

The streamlines of the flow from which 75 percent of the mean velocity has been subtracted shows roughly relative velocity field of the vortex, because the mean speed of the vortex center is observed to be about 75 percent of the mean flow (Atkinson, 1981). The vortex street can be only observed by cloud pattern in satellite pictures. The cloud pattern reflects relative velocity rather than absolute velocity, so that the subtracted streamlines can be comparable with these observation.

The subtracted streamlines emphasize vortices. Figure 6, which corresponds to Fig. 5e, but with the streamlines of total velocity, shows only the first two vortices. The third one has been quite deformed.

In the stably stratified atmosphere, turbulence derives from shear in the mean wind. The route by which the flow switches from the mean flow to a turbulent state is complex and poorly understood, but it is very likely that wave instabilities play an essential intermediate role (Chimonas, 1978). The wave breaking can be detected by a high values of vertical diffusivity, where maximum steepening of potential temperature isosurfaces is observed.

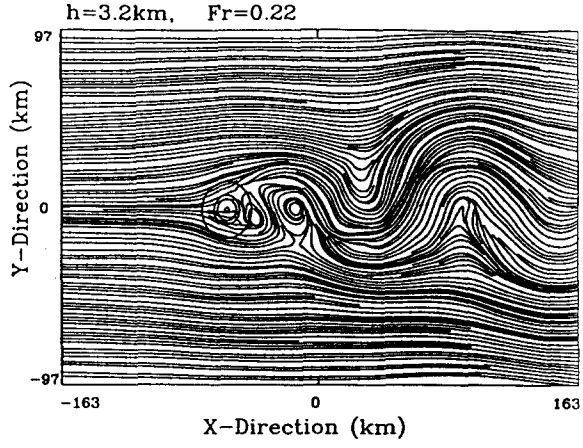

Fig. 6. The same as Fig. 5e, but for total velocity (without subtraction).

Figure 7 shows a vertical cross section of isentropes (thin solid line) and vertical diffusivity (thick solid line) in the case of Karman vortex (see Fig. 5e). As shown in this figure, the maximum diffusivity is obtained where the air is rising (hydraulic jumps) in the lee of the mountain. In the case of Karman vortex (see Fig. 5e), the maximum steepness of isentropes and the maximum concentration of vertical diffusivity are observed after the flow passed the bottom part of mountain (about 0.5 km height). Therefore, the possible wave breaking could be expected in that region. In this study, the onset of wave breaking is observed after Fr is less than 0.8 (see Fig. 8). At the onset of wave breaking, the vertical diffusivity increases significantly, reaching a typical value of 300 $m^2 s^{-1}$.

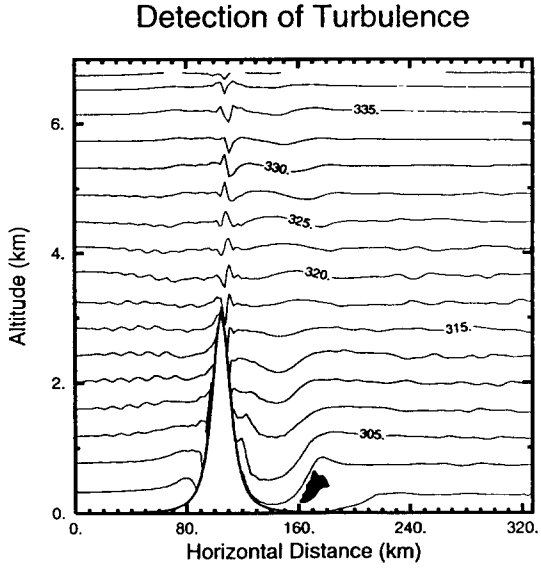

Fig. 7. The vertical cross section of isentropes and vertical diffusivity in the case of Karman vortex (see in the case e of both Fig. 5 and Fig. 8).

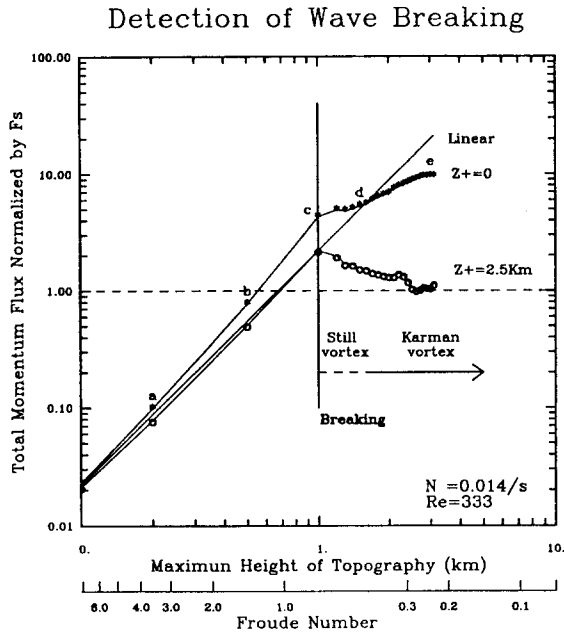

Fig. 8. Integrated momentum fluxes at the level of $z^+ = 0$ (i.e., at the surface; indicated by solid line (*)), $z^+ = 2.5$ km (solid line (o)) and the flux given by the linear theory as functions of the mountain height. Momentum fluxes were normalized by the saturated momentum flux F_S (see eq.8.1). Breaking point is the minimum mountain height over which turbulence is generated and the vertical diffusion occurs due to the wave breaking.

7. Momentum budget in z^+ coordinate system

Existence of vortices in the lee of the mountain implies that some drag of the mountain acts in the lower atmosphere in spite of no surface friction. This drag may be caused by the non-linear mountain waves. To investigate this, an estimate of the momentum budget is useful. To calculate the momentum budget, the following momentum equation of x component is used.

$$\frac{\partial u}{\partial t}+\frac{\partial uu}{\partial x^*}+\frac{\partial uv}{\partial y^*}+\frac{\partial uw^*}{\partial z^*} =$$
$$-\Theta\frac{\partial \Pi'}{\partial x}+g\frac{\theta'}{\Theta}\frac{\partial z_G}{\partial x^*}+\frac{\partial}{\partial z^*}(K_v\frac{\partial u}{\partial z^*})+\phi \ , \quad (7.1)$$

where ϕ represents horizontal viscosity terms operating in z^* coordinate. Here, the ambient wind velocity U and deviation u' are defined as:

$$u = U+u' \ , \quad (7.2)$$

where U is a constant.

Terrain-following coordinates system defined by eq. (2.6), however, is not convenient to estimate momentum budget though the numerical model is written in it. Therefore, another simpler terrain coordinate system is defined as follows:

$$x^+ = x \ , \ y^+ = y \ , \ z^+ = z-z_G \ . \quad (7.3)$$

Using this coordinate system, the momentum equation of x component (eq.7.1) is transformed to :

$$\rho\frac{\partial u}{\partial t} = \nabla^+ \cdot F \ , \quad (7.4)$$

where F is flux vector of x component momentum and defined by :

$$F/\rho=\begin{pmatrix} -uu' & -\Theta\Pi' \\ -vu' & \\ -w^+u'+ & \Theta\Pi'\frac{\partial z_G}{\partial x^+} \end{pmatrix}+\begin{pmatrix} 0 \\ 0 \\ K_v\frac{\partial u}{\partial z^+} \end{pmatrix}+\begin{pmatrix} H_x \\ H_y \\ H_z \end{pmatrix} . \quad (7.5)$$

where ∇^+ is the operator vector defined as :

$$\nabla^+ = (\frac{\partial}{\partial x^+} \ , \ \frac{\partial}{\partial y^+} \ , \ \frac{\partial}{\partial z^+}) \ . \quad (7.6)$$

The first term of the right hand side is momentum flux by the grid scale flow, which includes mountain waves. The second term in eq. (7.5) is the vertical viscosity term. The last term is the momentum flux by horizontal viscosity operating in z^+ plane, which is given by :

$$\begin{pmatrix} H_x \\ H_y \\ H_z \end{pmatrix}=K_H\begin{pmatrix} \frac{\partial u}{\partial x^+}+\alpha_x\frac{\partial u}{\partial z^+} \\ \frac{\partial u}{\partial y^+}+\alpha_y\frac{\partial u}{\partial z^+} \\ \alpha_x\frac{\partial u}{\partial x^+}+\alpha_y\frac{\partial u}{\partial y^+}+(\alpha_x^2+\alpha_y^2)\frac{\partial u}{\partial z^+} \end{pmatrix} , \quad (7.7)$$

where $\alpha_x = \frac{z^+}{z_T-z_G}\frac{\partial z_G}{\partial x}$, $\alpha_y=\frac{z^+}{z_T-z_G}\frac{\partial z_G}{\partial y}$.

Total momentum drag D of the mountain is given by z^+ component of $F(z^+=0)$ integrated in a large enough area including the mountain. Since w^+ and α are zero on the ground surface, D is given by:

$$D = \rho\Theta\int\int_{s^+}\Pi\frac{\partial z_G}{\partial x}ds^+ \ , \quad (7.8)$$

where boundary of integration area S^+ must be far enough from the mountain.

Integrated vertical momentum flux $\psi(z^+)$ caused by grid scale flow is defined by :

$$\psi(z^+) = \rho\int\int_{s^+}(-w^+u'+\Theta\Pi\frac{\partial z_G}{\partial x})ds^+ \ , \quad (7.9)$$

and total integrated vertical momentum flux $F_T(z^+)$ is given by :

$$F_T(z^+) =$$
$$\psi(z^+)+\rho\int\int_{s^+}K_v\frac{\partial u}{\partial z^+}ds^+ +\rho\int\int_{s^+}H_zds^+ . \quad (7.10)$$

On the other hand, the wave drag produced by the linear model is given by eq. (4.2).

8. Vertical momentum flux of the simulated flow

The effects of non-linear mountain wave caused by wave breaking can be detected by total integrated momentum fluxes normalized by

saturated momentum fluxes at two levels.

In Fig. 8, the total integrated momentum fluxes at the levels of $z^+=0$ and $z^+=2.5$ *km* ($\approx 3.5U/N$) are shown with stars (*) and open circles (*o*), respectively. The scales on the abscissa are the logarithm of the mountain height (top) and an inverse Fr number (bottom). In the figure, F_L, the integrated momentum flux given by the linear theory, is illustrated with a solid line. The line shows that F_L is proportional to the square of the mountain height.

As long as mountain height is less than about 900 *m*, momentum fluxes of numerical model (* and *o*) are close to the linear solution F_L. However, numerically computed fluxes increase more rapidly with mountain height than the analytical one. Rapid increase is likely due to nonlinearity of internal gravity waves. Momentum flux at the surface (*) is always larger than that at the level of 2.5 *km* (o), due to the effects of horizontal viscosity as explained earlier.

For a mountain higher than about 900 *m*, the vertical diffusivity increases over the mountain, since wave breaking occurs. As a result, the numerically computed momentum flux suddenly becomes different than the linear solution. Fr number at this point is a so called 'critical Froude number (Frc) and is estimated to be about 0.8 in this case. If Fr is less than Frc, internal waves can not any longer carry momentum as efficiently as linear waves do. The numerical results show that the rate of change of F_T(2.5 *km*) is negative or quite small, whereas F_T(0) still increases. The difference between F_T(0) and F_T(2.5 *km*) increases with mountain height. The difference implies that the horizontal velocity up to 2.5 *km* is to be decelerated in the lee of the mountain, forming horizontal wind shear.

According to linear theory, the total momentum flux of mountain waves, F_L, is proportional to the square of the mountain height. Due to the wave breaking (i.e., nonlinear effects), the mountain waves propagating into a stratified layer will be saturated with the maximum value of the momentum flux, which depends on N (Lindzen, 1981).

The magnitude of the saturated momentum flux is estimated to be the same order of magnitude as the linear flux for the mountain height for which Fr number is equal to 1. This mountain height is a minimum height which would generate wave breaking. This saturated momentum flux is estimated as:

$$F_s = \rho \frac{\pi}{4} \frac{u^3}{N} a \ . \qquad (8.1)$$

Figure 9 shows the total momentum flux normalized by the saturated momentum flux (F_s)

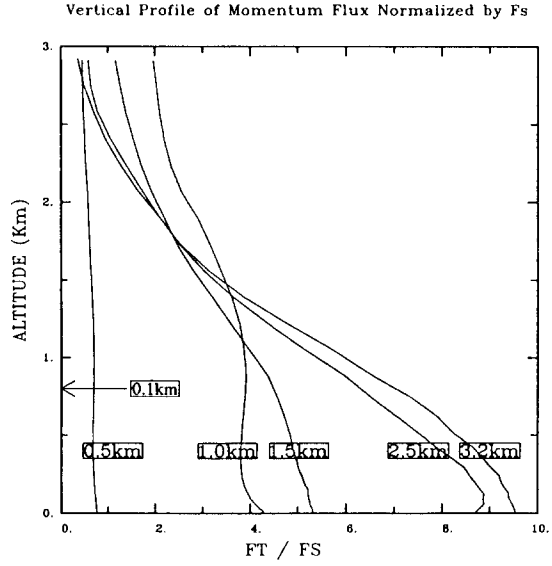

Fig. 9. Total (negative) momentum flux normalized by the saturated momentum flux F_S in cases of mountain height h=0.1, 0.5, 1.0, 1.5, 2.5 and 3.2 *km*.

for $h = 100$, 500, 1000, 1500, 2500, and 3200 m. When h is less than 500 m, i.e., Fr is larger than 1, F_T is almost constant with height. The values agree well with those given by the linear theory, although the flux is slightly larger than the linear one because of weak nonlinear effects (weak means non-breaking). For h larger than 1500 m, F_T at the surface is still increasing with height, but at levels over 3 km it is almost constant (about 1.2). At lower levels, the momentum flux is oversaturated and decreasing with height. It becomes almost saturated at the level of about 2 km (roughly equal to $\pi U/N$).

9. Conclusion

We have found that the numerical model can form Karman vortices in the lee of an isolated mountain without either surface friction or an elevated inversion. These findings agree with the results of Smolarkiewicz and Rotunno (1989), who explained this fact by a nonlinear and isentropic process. In this study, however, it was shown that the vortex formation is related to breaking of the mountain waves, which is not an isentropic process.

The vertical momentum flux by mountain waves in the upper level is subject to the wave saturation theory of Lindzen (1981). Namely, the flux can not exceed a saturated value which depends only on the ambient wind velocity and stratification N. The numerical results agree with this prediction in case of small Fr number. However, the surface mountain drag is several times larger than the saturated value. The magnitude of the momentum flux decreases with height and becomes almost constant, i.e., attains the saturated value at the level of about $\pi U/N$. As a result, large flux divergence is produced in the lower layer. The mean wind velocity is decelerated in the lee of the mountain, and the horizontal wind shear forms there. The momentum exchange between the mountain waves and the mean wind is caused by turbulent viscosity generated by the wave breaking. When the horizontal shear is strong enough, the Karman vortex will form by the barotropic instability as mentioned by Yagi et al. (1987). The onset of wave breaking is observed if Fr is less than 0.8 (see Fig. 8) in the numerical model, but it will depend on the shape of the mountain. The Karman vortex forms when Fr is less than about 0.22, although stationary lee vortices forms when Fr is larger. By analogy with the laboratory Karman vortex, in the previous studies horizontal viscosity of the atmosphere has been estimated by the frequency and the interval between eddies (Atkinson, 1981). However, the present results suggest that the formation mechanism in the atmosphere is different from that in the laboratory, so that the analogy mentioned above is doubtful.

The momentum budget calculated by hydrostatic model is almost the same as the nonhydrostatic result. Well developed Karman vortex similar to the hydrostatic result was simulated in the nonhydrostatic case. This means that the hydrostatic assumption is adequate for investigation of the origin of Karman vortex from the viewpoint of wave breaking.

Acknowledgements

This research was carried out as a part of the special research project on global environmental change in University of Tsukuba. This research was supported by a Grant-in-Aid for Scientific Research, the Ministry of Education, Science, and Culture, No. 08454128.

References

Atkinson, B. W., 1981: Meso-scale Atmosphere. Academic Press, pp 495.

Bougeault, P. 1983: A non-reflective upper boundary condition for limited-height hydrostatic models. Mon. Wea. Rev., 111, 420-429.

Brighton, P. W. M., 1978: Strongly stratified flow past three dimensional obstacles. Quart. J. Roy. Met. Soc., 104, 289-307.

Chimonas, G., and C. J. Nappo, 1989: Wave drag in the planetary boundary layer over complex terrain. Boundary-Layer Meteorol., 47, 217-232.

Chopra, K. P. and L. F. Hubert, 1965: Mesoscale eddies in Wake of Island. J. Atmos. Sci., 22, 652-657.

Durran D. R., 1995: Do Breaking Mountain Waves Decelerate the Local Mean Flow ?. J. Atmos. Sci., 52, 4010-4032.

Harada, A., 1981: An Analysis of the Nocturnal Cyclonic Vortex in the Kanto Plains. J. Meteor. Soc. Japan, 59, 602-610.

Hubert. L. F. and A. F. Kruger, 1962: Satellite picture of mesoscale eddies. Mon. Wea. Rev.}, 90, 457-463.

Kikuchi, Y., S. Arakawa, F. Kimura, K. Shirasaki and Y. Nagano, 1981: Numerical Study on the Effects of Mountains on Land and Sea Breeze Circulation in the Kanto District. J. Meteor. Soc. Japan, 59, 723-737.

Kimura, F., 1986: Formation Mechanism of the Nocturnal Mesoscale Vortex in Kanto Plain. J. Meteor. Soc. Japan, 64, 857-870.

Kimura, F. and S. Arakawa, 1983: A Numerical Experiment on the Nocturnal Low Level Jet over the Kanto Plain. J. Meteor. Soc. Japan, 61, 848-861.

Klemp, J. B. and D. R. Durran, 1983: An Upper Boundary Condition Permitting Internal Gravity Wave Radiation in Numerical Mesoscale Models. Mon. Wea. Rev., 111, 430-444.

Lindzen, R. S., 1981: Turbulence and Stress Owing to Gravity Wave and Tidal Breakdown. J. Geophy. Res., 86, C10, 9707-9714.

McGregor, J. L. and F. Kimura, 1989: Numerical Simulation of Mesoscale eddies over Melbourne. Mon. Wea. Rev., 117, 50-66.

Olafsson H. and P. Bougeault, 1996: Nonlinear Flow Past an Elliptic Mountain Ridge. J. Atmos. Sci., 53, 2465-2489

Olafsson H. and P. Bougeault, 1997: The Effect of Rotation and Friction on Orographic Drag. J. Atmos. Sci., 54, 193-210.

Orlanski, I., 1976: A simple boundary condition for unbounded hyperbolic flows. J. Comp. Phys., 21, 251-269.

Ruscher, P. H. and J. W. Deardorff, 1982: A Numerical Simulation of an Atmospheric Vortex Street. Tellus, 34, 555-566.

Satomura, T., 1986: Topographic Disturbance in Viscous Shear Flow. J. Meteor. Soc. Japan}, 64, 665-680.

Schar C. and D. R. Durran, 1997: Vortex Formation and Vortex Shedding in Continuously Stratified Flows past Isolated Topography. J. Atmos. Sci., 54, 534-554.

Smolarkiewicz, P. K. and R. Rotunno, 1989: Low Froude Number Flow Past Three-Dimensional Obstacles. Part I: Baroclinically generated lee vortices. J. Atmos. Sci., 46, 154-1164.

Smith, R. B., 1980: Linear Theory of Stratified Hydrostatic Flow Past an Isolated Mountain. Tellus, 32, 348-364.

Smith R. B. 1989: Comment on low Froude number flow past three-dimensional obstacles. Part I: Baroclinically generated lee

vortices. J. Atmos. Sci., 46, 3611- 3617.

Smith R. B., and S. Gronas, 1993: Stagnation points and bifurcation in 3-D mountain airflow. it Tellus, 45A, 28-43.

Spelt C. and Etling D., 1989a: On Atmospheric Vortex Streets in the Wake of Large Islands. Submitted to Meteorol. Atmos. Phys.

Spelt C. and Etling D., 1989b: Mesoscale Vortex Shedding from Large Islands. Submitted to Meteorol. Atmos. Phys.

Tsuchiya, K., 1969: The Clouds with the Shape of Karman Vortex Street in the Wake of Cheju Island. J. Meteor. Soc. Japan, 47, 457-465.

Yagi, S., F. Kimura and S. Takahashi, 1987: Karman Vortex in the Atmosphere: Analysis, Consideration and Numerical Experiment with Two-Layer Model (in Japanese), Proceedings of Annual Meeting of Japan Meteor. Soc., Oct, 1987.